Quantification of Collagen Fiber Structure using Second Harmonic Generation Imaging and 2D Discrete Fourier Transform Analysis: Application to the Human Optic Nerve Head

Authors: Jacek K. Pijanka[1*], Petar P. Markov[1*], Dan Midgett[2,3], Neil G. Paterson[4], Nick White[5], Emma J. Blain[6], Thao D. Nguyen[2,3], Harry A. Quigley[7], Craig Boote[1]

Author information:

1) Structural Biophysics Group, School of Optometry and Vision Sciences, Cardiff University, CF24 4HQ, Cardiff, UK
2) Department of Mechanical Engineering, The Johns Hopkins University, Baltimore, MD 21218, USA
3) Department of Materials Science, The Johns Hopkins University, Baltimore, MD 21218, USA
4) Diamond Light Source, Harwell Science and Innovation Campus, Harwell, UK
5) Vivat Scientia Bioimaging Labs, School of Optometry and Visual Sciences, Cardiff University, CF24 4HQ, Cardiff, UK
6) Arthritis Research UK Biomechanics and Bioengineering Centre, Cardiff University, CF10 3AX, Cardiff, UK.
7) Wilmer Ophthalmological Institute, School of Medicine, The Johns Hopkins University, Baltimore, MD 21287, USA

*These authors contributed equally

Correspondence to: Craig Boote, PhD
School of Optometry and Vision Sciences
Cardiff University
Maindy Road
Cardiff CF24 4HQ
UK
Email: bootec@cardiff.ac.uk

Key words: Non-linear microscopy, Second Harmonic Generation, Discrete Fourier Transform, edge effect artefact correction, collagen fiber structure, optic nerve head

This article has been accepted for publication and undergone full peer review but has not been through the copyediting, typesetting, pagination and proofreading process, which may lead to differences between this version and the Version of Record. Please cite this article as doi: 10.1002/jbio.201800376

Abstract

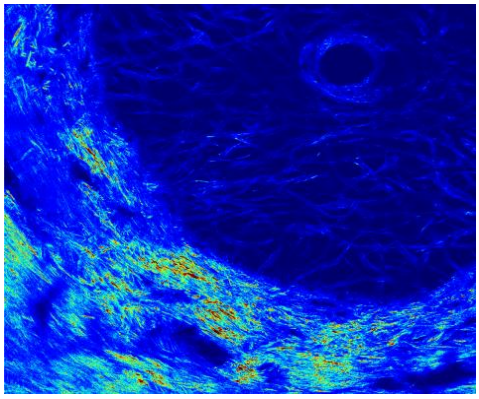

Second Harmonic Generation (SHG) microscopy is widely used to image collagen fiber microarchitecture due to its high spatial resolution, optical sectioning capabilities and relatively non-destructive sample preparation. Quantification of SHG images requires sensitive methods to capture fiber alignment. This paper presents a 2D Discrete Fourier Transform (DFT) based method for collagen fiber structure analysis from SHG images. The method includes integrated Periodicity Plus Smooth Image Decomposition (PPSID) for correction of DFT edge discontinuity artefact, avoiding the loss of peripheral image data encountered with more commonly used windowing methods. Outputted parameters are: the collagen fiber orientation distribution, aligned collagen content and the degree of collagen fiber dispersion along the principal orientation. We demonstrate its application to determine collagen microstructure in the human optic nerve head, showing its capability to accurately capture characteristic structural features including radial fiber alignment in the innermost layers of the bounding sclera and a circumferential collagen ring in the mid-stromal tissue. Higher spatial resolution rendering of individual lamina cribrosa beams within the nerve head is also demonstrated. Validation of the method is provided in the form of correlative results from wide-angle X-ray scattering (WAXS) and application of the presented method to other fibrous tissues.

1 Introduction

Collagen is the most abundant family of proteins in the human body, with more than 20 different types characterized. Molecules of fibrous collagens, such as type I, assemble to form strong and flexible fibrils which, in turn, gather to form higher-order structures including fibril bundles and fibers. Microarchitecture of collagen fibers, particularly their orientation and content, plays a major part in determining the biomechanical properties of biological tissues.

In the sclera, the white fibrous tissue of the eyeball coating and its principal load-bearing component, a complex network of collagen fibers provides the necessary mechanical strength to sustain the intraocular pressure (IOP) and largely defines the eyeball's response to changes in internal pressure and external forces [1, 2]. Near the posterior pole of the eye a specialized, fenestrated extension of the scleral tissue, called the lamina cribrosa, facilitates and supports the exiting retinal nerve axons as they gather to form the optic nerve [3]. The lamina cribrosa and its immediate neighbouring scleral tissue, the peripapillary sclera (PPS), collectively form the connective tissue component of the optic nerve head (ONH) – the mechanical properties of which play an important role in the blinding disease glaucoma, where deformation of the ONH tissues may lead to axonal injury and subsequent death of neural cells [3-5]. Significant experimental and modelling research has been conducted on the biomechanical properties of these tissues, namely their physical response to changes in IOP and their role in determining susceptibility to glaucomatous damage [6-11]. More specifically, computational studies have demonstrated the importance of the collagen fibrillar architecture of the PPS as a substantial factor determining IOP-induced deformation of the ONH [12, 13].

A large array of imaging and other techniques have been utilized to both qualitatively and quantitatively assess the structure of the ocular collagen fiber network at different levels of organisation. These include electron microscopy [2, 14], polarization light microscopy [15, 16], small-angle light scattering ([17, 18]) and wide-angle X-ray scattering (WAXS) [19, 20]. Since the early 2000's second harmonic generation (SHG) microscopy has evolved as a useful imaging tool for imaging the suprafibrillar assembly of the collagen network in various connective tissues, including skin [21, 22], tendon [23, 24], muscle [25], cornea [26], sclera [27, 28] and cardiovascular tissue [29, 30]. It has also been successful in detecting and quantifying the

effects of various deleterious connective tissue conditions and insults, such as corneal photothermal damage [31], keratoconus [32], heat burns [33, 34], matrix remodelling in tumour microenvironments [35-37], as well as tissue fibrosis [38] and scarring [39].

SHG is a coherent, non-linear scattering process where the combined energy of two photons, made to arrive virtually simultaneously at an appropriate molecular structure, is scattered as a single photon at exactly half the wavelength of the incident photons. SHG is only exhibited by non-centrosymmetric molecules such as fibrillar collagen, myosin and tubulin, and the process only occurs at the focal plane of the laser beam, allowing fine and deep-penetrating optical sectioning, even in turbid samples. Moreover, due to the intrinsic nature of SHG emission, no tissue labelling or sectioning is required [40, 41]. Together these factors allow for non-destructive, high spatial resolution imaging of fibrous collagen-rich connective tissues in three dimensions.

In recent years, the increasing move towards combined computational and experimental methods to model connective tissue mechanical behaviour has driven the development of more quantitative imaging approaches to measure the orientation and content of collagen fibers visualized through various imaging modalities, including SHG. One group of methods is based on a matrix of partial derivatives along image x-y directions called structure tensors. They enable calculation of numerous orientation parameters including fiber preferential orientation and degree of anisotropy [42]. In addition, fibre analysis plugin algorithms have been developed for the open source image processing software Image J, such as Orientation J and FibrilTool [43, 44]. Other standalone methods such as CT-FIRE enable detection and tracking of individual fibers within an image, allowing reconstruction of collagen network architecture and extraction of fiber-level parameters including length, diameter, number and orientation [45-48].

The most commonly used approach for quantifying collagen organization and anisotropy from microscopy images are those based on the analysis of the spatial frequencies in image pixel intensities computed using Discrete Fourier Transform (DFT) method. Notably this approach has been found to be superior in detecting directionality of fibrillar structures when compared to other techniques such as mean intercept length and line fraction deviation methods [49]. Several approaches have been adopted to calculate the dominant fiber orientation and

anisotropy from the DFT patterns, the most common being ellipse fitting to the power spectrum [31, 50, 51], and to extract directly the magnitude of the frequency components as an angular fiber distribution [39, 52, 53].

In this paper we describe the use of SHG imaging together with a bespoke, automated image analysis processing technique, based on DFT, as a reliable approach to quantitatively characterize collagen fiber organization. We demonstrate the application of the method using human ONH tissue as a model system. Angular fiber distribution, aligned fiber content and the degree of fiber recruitment around the preferred orientation are computed from the DFT power spectrum and plotted as spatial maps. Characteristic collagen fiber distributions through the thickness of the ONH are presented and validated by correlation with results from an established WAXS method. Notably, our presented method involves the application of an image decomposition algorithm to correct DFT edge artefact that is shown to result in superior preservation of peripheral image information compared to more commonly used windowing methods. Finally, we compare the method presented here with alternative approaches to SHG image quantification with and without DFT, and demonstrate its potential for adaptation to other imaging modalities and tissues.

2 Materials and Methods

2.1 Ethical statement

All experimental procedures involving human tissue were performed in accordance with the WMA Declaration of Helsinki on Ethical Principles for Medical Research involving Human Subjects. Ethical approval for the use of human specimens in the study was granted at local (School of Optometry & Vision Sciences School Research Ethics Committee) and national (NHS-HRA Wales Research Ethics Committee) levels. All experiments involving animal tissue were carried out in accordance with the ARVO Statement for the use of Animals in Ophthalmic and Vision Research. Maintenance and experimental handling of live chickens and rats from which tissue were harvested was performed under Home Office licenses held by the Roslin Institute and Cardiff University, respectively.

2.2 Specimen preparation

Two human eyes from two different Caucasian donors (ages 86 and 69) were obtained from the National Disease Research Interchange (NDRI) and Bristol Eye Bank (UK), respectively, within 48h post-mortem. Appropriate donor consents were obtained locally by eye banks. The extraocular (cornea, anterior sclera) and intraocular (retina, choroid) tissues were removed, and the optic nerve excised with a razor blade flush to the sclera. The scleral specimens were fixed while in their natural curvature by immersion in 4% paraformaldehyde (PFA) solution in 1 x phosphate buffered saline (PBS). The anatomical orientation was marked on each eye and a circular specimen of 10 – 12mm, centred around the ONH, was excised with fine scissors. These tissue buttons were subsequently cut into six or seven 150 μm thick serial sections using a sledge cryo-microtome (HM440E, Microm, Walldorf, Germany). Each section was mounted on a microscope slide in a 1:1 mixture of PBS/glycerol to maintain tissue hydration and minimise refractive index mis-matching [17, 20], with the innermost surface (proximal to choroid) facing the incoming laser beam. The specimens were covered with glass coverslips, and their edges sealed with clear nail varnish. Following SHG imaging, sections were removed from the slides, briefly washed in PBS and stored in 4% PFA solution at 4^{o}C, while awaiting WAXS experiments.

2.3 SHG image collection

For SHG imaging, slide mounted specimens in 1:1 PBS/glycerol mixture were used. Non-linear laser scanning multiphoton microscopy was performed using a Zeiss LSM 880 META NLO microscope (Carl Zeiss Ltd, Welwyn Garden City, UK). SHG signals from fibrous collagen were generated using an ultrafast titanium-sapphire tuneable infrared (680-1080nm) laser (Cameleon Vision II; Coherent, Inc., Ely, UK) operating at 800nm (140fs pulse duration, 80 MHz repetition rate), and detected in the forward scattered direction after passing through a 400nm (bandwidth 6nm) filter [30]. The excitation laser was focused on the sample using a W Plan- Apochromat 20× 1.0N.A. DIC (D=0.17) water immersion objective lens, resulting in a 425μm × 425μm field of view (FOV) per tile before stitching. Scan zoom setting was 1.0 x. A 9 × 9 FOV tiling covering, in total, a 12.25 mm^2 area of the specimen (after tile stitching), was obtained using a motorized x-y stage. Each single FOV frame was recorded at 512 x 512 pixel resolution, while averaging each line of the frame twice. Pixel size was 0.83 μm –

corresponding to the maximum lateral resolution of 1.6 μm, with a dwell time of 1.03 μs per pixel. Optical sections through the full thickness tissue were obtained at z-intervals of 25 μm. Laser power was increased between 1.5% (top of sample) to 7.5% at a depth of 150 μm in order to partially compensate for the reduction in detected signal due to scattering/reflection and residual spherical aberration at deeper tissue depths. 8-bit images were recorded with non-descanned NDD2 detectors and saved in ".CZI" Zeiss file format. Complete image tilings were obtained post-imaging by stitching individual FOV tiles using Zen Blue software with a 10% tile overlap.

2.4 SHG image processing and analysis

A bespoke analysis routine was developed in MATLAB software (MathWorks Inc., Natick, USA). Image files were loaded as a cell array, from where the desired signal channel and optical slice from an image z-stack was accessed. Stitched SHG image tilings were partitioned into individual tiles for DFT analysis of a user-defined dimension appropriate to the length-scale of the structure of interest. In the analysis of ONH tissues presented herein, we demonstrate DFT analysis at various spatial resolutions ranging from 256 ×256 pixel tiles for regional averaging of continuous scleral tissue, to 16 × 16 pixel tiles for analysis of the narrow tissue beams in the porous lamina cribrosa tissue.

2.4.1 FFT generation

The Fourier transform is widely used in image processing applications such as image reconstruction, filtering methods, file compression or texture analysis - arising from the fact that such tasks are most effectively performed in the frequency domain. 2D DFT transforms spatial information in an image into the frequency domain; that is, it decomposes the image contents into a superposition of orthogonal spatial frequency (sine and cosine) components along horizontal and vertical axes. These spatial frequencies indicate the rate at which pixel intensities change in the spatial domain. In images of fibrous tissues, following abrupt changes in intensity across the image at fiber edges allows tracking of the fiber orientation. For an input image *f(x, y)* of size M x N pixels, where *x* and *y* are the row and column dimensions of *f(x, y)*, the 2D discrete Fourier transform (DFT) can be expressed as

$$F(u,v) = \sum_{x=0}^{M-1}\sum_{v=0}^{N-1} f(x,y) \cdot \exp\left[-j2\pi\left(\frac{ux}{M}+\frac{vy}{N}\right)\right] \quad (1)$$

where *u = 0, 1, 2, …, M-1* and *v = 0, 1, 2, …, N-1* are the variables in the frequency domain.

The 2D DFT of an image is an array of complex numbers, so the way to analyse it visually is to compute its spectrum, that is the magnitude of $F(u,v)$, and display it as an image.
The power spectrum $P(u,v)$ is then defined as the square of the magnitude:

$$P(u,v) = |F(u,v)|^2 = R^2(u,v) + I^2(u,v) \quad (2)$$

Where $R(u,v)$ and $I(u,v)$ are the real and imaginary components of $F(u,v)$.

We used the MATLAB function *fft2* to compute a 2D DFT for each partitioned tile. For visualization, the DFT results were shifted so that the zero-frequency components were at the centre of the figure using the function *fftshift*.

To further improve visualization, the large dynamic range of values in the power spectrum was handled by applying a logarithmic transformation, e.g. $\log(1 + abs(FT_{Result}))$.
Here *abs* is the function that computes the magnitude of each complex element of the transformed array [54, 55].

2.4.2 Edge artefact correction

DFT analysis requires an image to be periodic at its edges. Since regular images are not periodic, the discontinuity across the frame edge introduces a centrally positioned cross-shaped artefact in the frequency domain [56]. To correct this, the use of an apodization windowing function to enforce a smooth transition at the image borders has been widely adopted [39, 49, 57]. A Hanning window is a commonly utilized method, which is a cosine-based function that smoothly reduces the signal to zero at the image edges, and is given by:

$$A(x) = \cos^2\left(\frac{\pi x}{2a}\right) = \frac{1}{2}\left[1 + \cos\left(\frac{\pi x}{a}\right)\right] \quad (3)$$

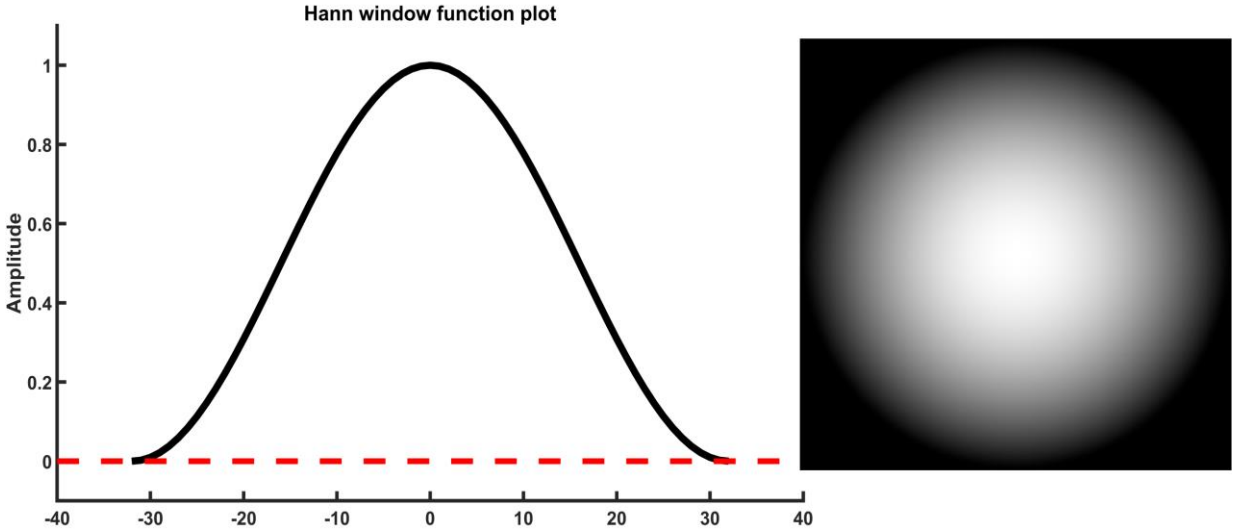

Figure 1 Plot of the Hann window function (left) and its image at a resolution of 256 x 256 pixels (right).

For apodization correction, the function was applied by multiplying the initial image (i.e. in the spatial domain) with a Hanning window of matching size (Figure 1, right), generated using ImageJ macro 'Hanning Window' [58]. However, ramping down of pixel intensity in the image border results in significant loss of peripheral information, which is especially a problem when small image tiles are required for fine spatial sampling of an image. Therefore, in the current work we also explored an alternative approach involving the decomposition of an image into a sum of its periodic and smooth components - the method known as the Periodicity Plus Smooth Image Decomposition (PPSID). The periodic component contains most of the visual content of the image along with the all the necessary data that enables the discrete Fourier transform to be performed, but does not yield the edge artefact. The smooth component is computed directly from the 'boundary image' by solving Poisson's equation, and it contains mostly the edge discontinuities which gives rise to the artefact in the Fourier domain. Subtracting this component from the original image removes the edge discontinuities while retaining most of the visual information [56, 59]. For Moisan's PPSID method, we used the MATLAB function *perdecomp*, available on the author's website (http://www.mi.parisdescartes.fr/~moisan/). We then assessed the resulting retention of original image information by examination of the

inverse Fourier transform of the corrected (i.e. periodic component) image, and compared it to the corresponding results from the Hanning apodization window method.

2.4.3 Fiber orientation analysis

The centro-symmetric DFT power spectrum contains amplitudes of the frequency components. These frequencies relate to the sizes of the structural features in the image, such that lower frequencies defining larger structures are closer to the origin and higher frequencies defining smaller features are further away. The angular location of peaks in the power spectrum relate orthogonally to the orientation of the corresponding features in the spatial domain.

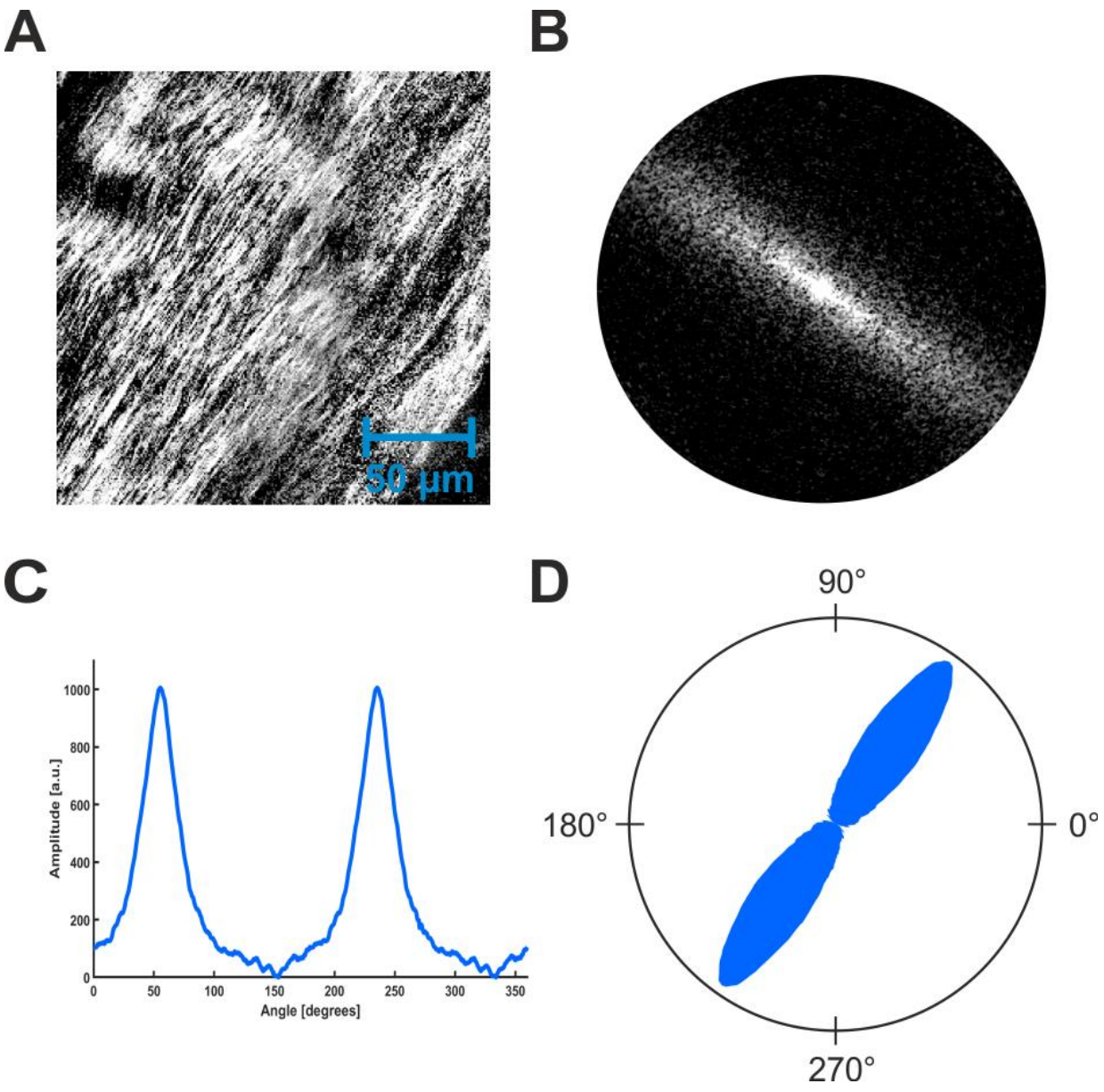

Figure 2 Obtaining fiber orientation from an SHG image. (A) SHG image of a collagen fibers within human PPS tissue. (B) Power spectrum of the image presented in (A) resulting from 2D Discrete Fourier Transform. (C) Angular distribution plot of the radially-integrated power spectrum, shifted 90 degrees to represent the fiber orientation distribution. (D) Corresponding polar vector plot of (C).

The 2D power spectrum was integrated radially and its values were placed into 0.5^{o} angular bins. Displaying these values as a line plot, and incorporating a 90° shift, yields the fiber orientation distribution (Figure 2C).

By displaying the phase-shifted angular power distribution data in polar coordinates, the fiber structure in each partitioned tile in the image was represented by a vector plot (Figure 2D), indicating the direction of preferred fiber orientation (angle of the longest vector) and the anisotropy (longest vector magnitude). Individual polar plots were assembled into montages showing the preferential fiber orientation across the specimen (Figures 6B and 7B).

The MATLAB function *findpeaks* was employed to automate the extraction of peak information, specifically: peak height values (anisotropy), the peak full width at half maximum (FWHM) and the angular position of the largest peak (Figure 3). For the largest peak, the ratio of the peak height to the FWHM was then computed as the degree of fiber recruitment (DFR) for the main collagen fiber direction. The MATLAB function *peakprominence* was used to filter out noise-related peaks from the analysis.

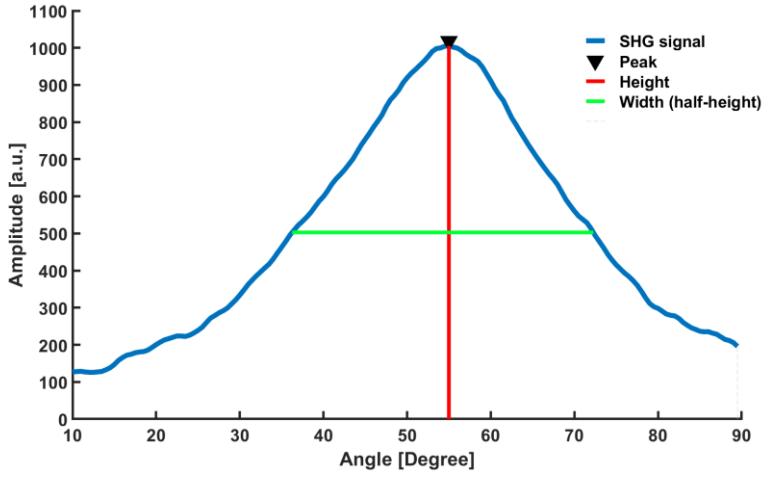

Figure 3 Analysis of peaks of SHG intensity emission from collagen fibers, using Matlab function *findpeaks*.

The variation in the aligned collagen fiber content across the specimen was determined by computing the integral of the angular frequency distribution for each tile, and assimilating these results into spatial maps (Figures 6C and 7C). A similar spatial map was also obtained for DFR of the main collagen direction (Figures 6D and 7D). Detection and removal of non-tissue regions in the aligned collagen and DFR maps was achieved by integrating the total SHG signal per tile and setting a low-intensity "background" threshold based on the average value of tiles located within known non-collagen regions – e.g. the inside of blood vessels (Figure 4B).

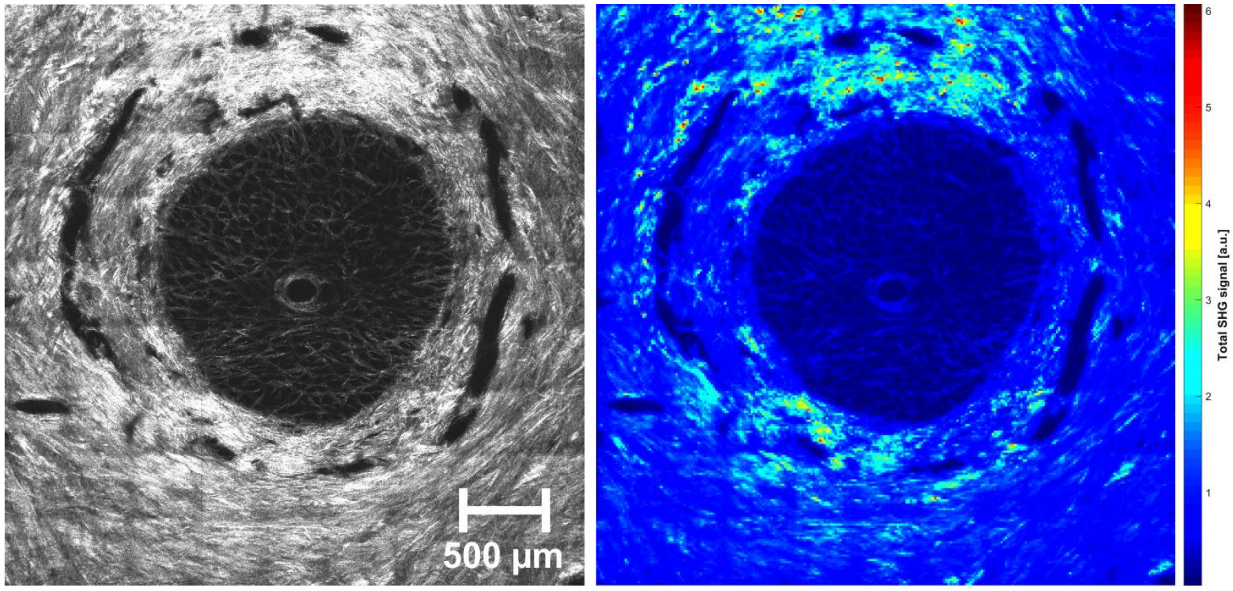

Figure 4 (A) SHG image tiling of a mid-stromal section through the human ONH. (B) Corresponding spatial map of total SHG signal per sampled tile. Resolution of sampled tiles is 16 x 16 pixels.

2.5 X-ray scattering data collection

For validation of our SHG analysis results, correlative WAXS experiments were conducted on macromolecular crystallography beamline I03 at the Diamond Light Source synchrotron facility (Harwell, UK), custom-adapted for fiber diffraction. The experimental protocol has been described in detail previously [60, 61]. During X-ray exposure, each specimen was wrapped in polyvinylidene chloride film to prevent dehydration, and mounted inside Perspex® (Lucite Group Ltd, Southampton, UK) chambers with Mylar® (DuPont-Teijin, Middlesborough, UK) windows. The incident X-ray beam of wavelength 0.09795nm and cross-section

dimensions of approx. 150 x 80 µm was directed perpendicular to the inner surface of each section. WAXS patterns resulting from an X-ray exposure of 2s were recorded on a Pilatus-6MF silicon pixel detector (Dectris Ltd, Baden, Switzerland) positioned 350mm behind the specimen position. For every specimen, WAXS patterns were recorded in a square grid pattern across the specimen at 0.25mm horizontal and vertical sampling intervals, with specimen translation between exposures achieved using an electronic x-y motor stage interfaced with the X-ray camera shutter.

2.5.1 X-ray data analysis

The collagen equatorial WAXS pattern is formed perpendicular to the fibril axis and arises from scatter from the regular 1.5-1.6 nm lateral spacing of collagen molecules, aligned near axially within the fibrils [19]. This scatter pattern represents an experimentally determined Fourier transform of the collagen fiber structure. WAXS is a well-established method for quantitative analysis of the collagen fiber orientation and anisotropy within connective tissues, including sclera [60-62]. Polar vector plots of collagen fiber preferred orientation and anisotropy, mirroring our SHG orientation analysis approach, were obtained from the WAXS patterns using a custom-developed MATLAB code following methods described elsewhere [63].

2.5.2 Correlation between WAXS and SHG collagen fiber orientation data

In order to assess how closely our method was able to represent the collagen fiber features in comparison with WAXS, the angular fiber distributions from each method were correlated point-for-point using the correlation function given in Equation 4:

$$C(S,X) = \frac{\sum_{i=1}^{721}(S_i-\bar{S}_i)(X_i-\bar{X}_i)}{\sqrt{(\sum(S_i-\bar{S}_i)^2\sum(X_i-\bar{X}_i)^2)}} \quad (4)$$

where S_i and X_i are the corresponding aligned scatter values for the integrated SHG map and WAXS map respectively, within each angular bin, i. The coefficient $C(S,X)$ compares the shape of the fiber polar plots (relating to the preferred fibril directions and associated dispersion), while ignoring the overall size of each plot (related to the anisotropy). Each correlation yielded a coefficient value between -1 and +1 that revealed how closely matched the preferred directions were, with a more positive value indicating similarity and a more negative value indicating difference.

3 Results

3.1 Comparison of DFT edge artefact correction methods

As mentioned, transforming SHG images into the frequency domain results in a characteristic cross-like artefact centred across the FT pattern due to the step transition at the tile edge. This artefact manifests as an erroneous sharp peak in the resulting angular distribution plots (Figures 5D and E). Two methods to correct this issue were compared in the present study: firstly, the widely used apodization windowing function method and, secondly, a recently developed Periodic plus Smooth Image Decomposition (PPSID) method. Both filter types were applied in the spatial domain. To our knowledge, the latter method has not been applied previously in fiber structure analysis. For apodization correction, a Hanning window function (Figure 1) was multiplied to the initial image in order to gradually ramp-down the peripheral image intensity and obtain a smooth transition at the tile edge. While this is effective in removing the cross artefact, it also results in a significant loss of peripheral image data. Moreover, when applied to the SHG fiber images, a notable reduction in overall amplitude of the orientation distribution is evident, as well as changes to the peak shapes (Figures 5 B, D and E). Technical details of the PPSID function method can be found elsewhere [59]. Application of PPSID to the SHG image tiles resulted in subtle regional changes to signal contrast in the image periphery, however the main image features remained largely unchanged. Moreover, the orientation distribution peak shape and overall amplitude were far more well-preserved than for the apodization method (Figures 5D and E). Accordingly, we incorporated the PPSID function into our SHG fiber analysis for subsequent quantification of the ONH collagen fiber structure.

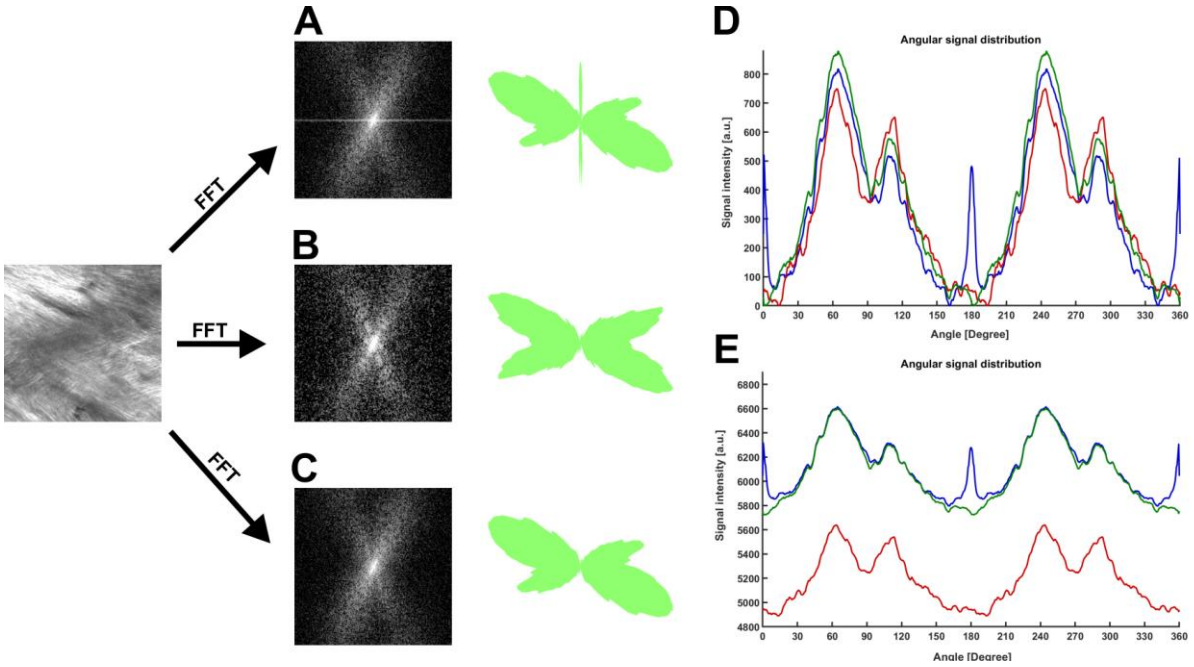

Figure 5 Comparison of different DFT edge artefact correction methods on fiber orientation data. (A) The results of DFT on the polar vector plots without any edge correction applied. (B) The effect of Hanning window function – note changes to polar plot lobe shapes. (C) The effect of PPSID function – note lobe shapes are better preserved than in (B). (D) Comparison of angular power distribution for all three methods. (E) Angular distribution profiles without the background component removed showing the overall drop in amplitude from lost peripheral data in the windowing function method. For (D) & (E): blue – no correction; red – Hanning window method; green – PPSID method.

3.2 Collagen fiber structure of the human ONH

To assess the capability of the presented method in determining fiber architecture from SHG microscopy images, we analysed collagen structural features within the human ONH – a connective tissue that exhibits features previously well-characterised using other scattering [20, 61] and imaging [16, 64] methods.

Figure 6B shows a polar vector map of collagen fiber preferred orientation in the innermost layers of the ONH posterior, approximately 220 μm from the choroid, sampled at 128 x 128 pixel resolution. The shape of the polar plots indicates that the majority of collagen fibers in the peripapillary sclera are orientated radially, with the exception of a narrow band of circumferential collagen immediately adjacent to the canal edge, in agreement with previous scleral results from WAXS [65] and polarized light microscopy [64] studies. The polar plot color variation discloses changes in anisotropy degree across the tissue. Note that, at this depth, the section plane through the ONH only captures part of the lamina cribrosa tissue

(Figure 6A). This can be explained by the fact that the lamina cribrosa inserts into the mid-to-outer depth of scleral stroma [66, 67] and hence would have curved in and out of the flat section plane through the inner scleral tissue.

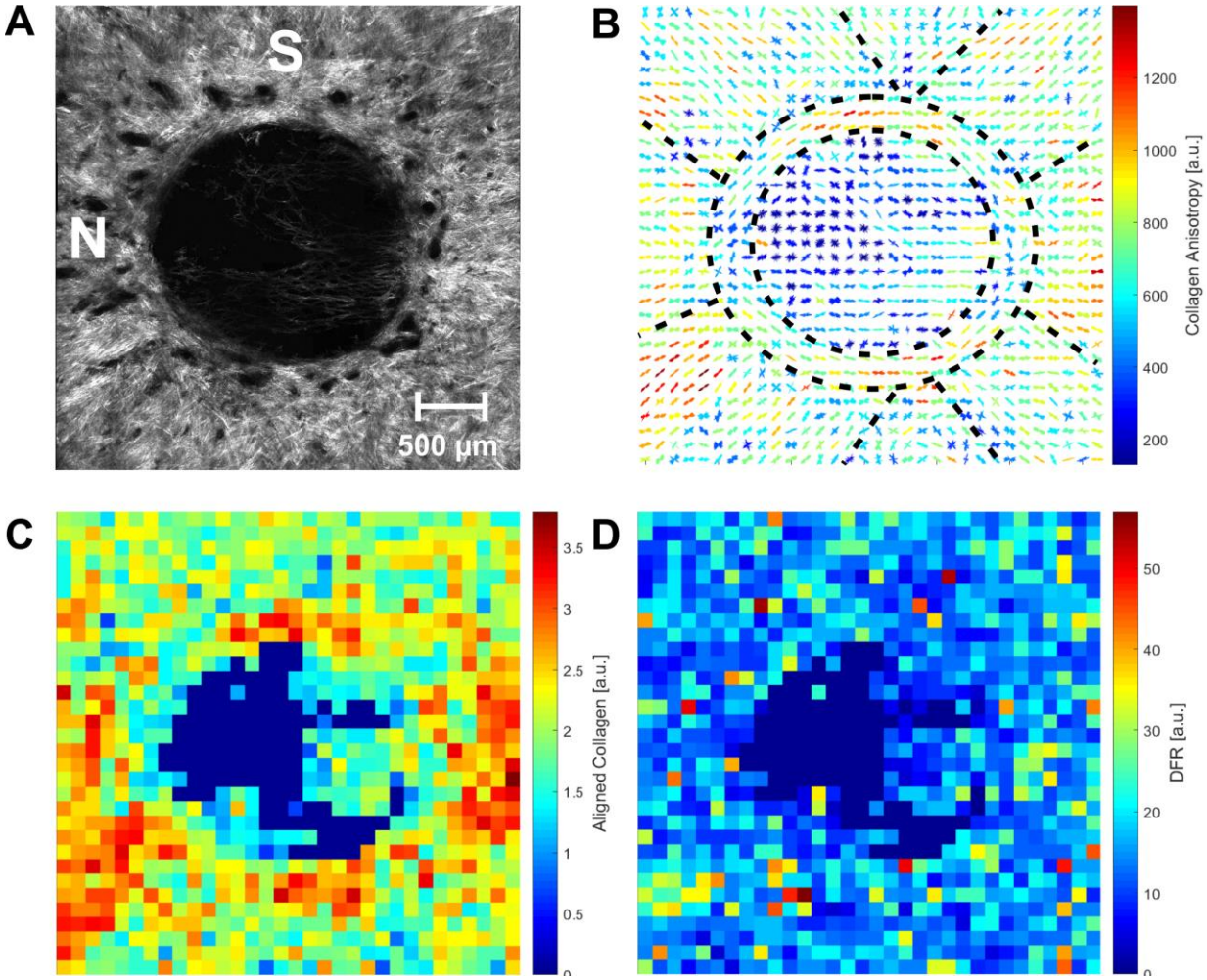

Figure 6 (A) SHG image of a section of the human ONH region and posterior sclera located approximately 220 µm from the choroid. S – superior, N – nasal. (B) Corresponding polar vector map of preferential collagen fiber orientation across the specimen, sampled from tiles of 128 x 128 pixels. Broken lines delineate the main collagen features. (C) Map of aligned collagen content. (D) Map of degree of fiber recruitment (DFR) for main collagen direction.

In the mid-depth ONH section (Figure 7A) a largely circumferential collagen structure in the PPS is clearly present, again in good agreement with previous studies [20, 64]. Moreover, a full section through the LC collagen beams is observed, with the polar plots showing the collagen fibers aligned approximately radially, reflecting the general lamina beam organization, and also seen to circumscribe the central artery (Figure 7B).

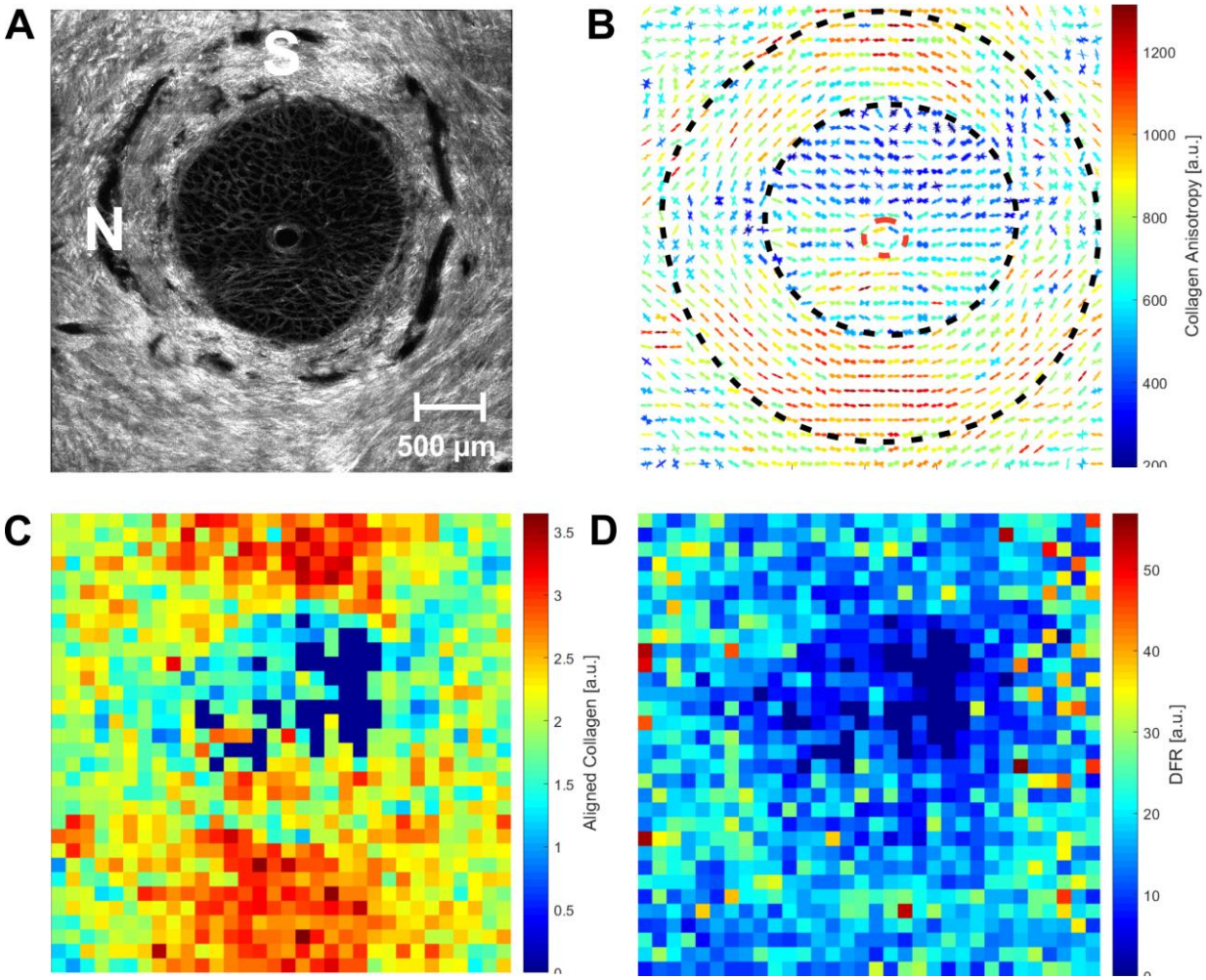

Figure 7 (A) SHG image of a mid-stromal section through the human ONH and posterior sclera, located approximately 520 µm from the inner surface. (B) Polar vector map of preferential collagen fiber orientation across the specimen, sampled from tiles of 128 x 128 pixels. Broken lines delineate the main collagen features. (C) Aligned collagen map. (D) Map of degree of fiber recruitment (DFR) for main collagen direction.

An adjacent mid-depth optical section of the same specimen was processed at finer resolution, using a smaller DFT tile sizes of 32 x 32 pixels (polar plots) and 16x16 pixels (aligned collagen content and DFR). The polar vector map confirms previous findings with greater detail but, also reveals more intricate features of the collagen fiber organization, including the detailed shape of blood vessels in the PPS from low scatter regions (Figure 8B). At this resolution, the method is also capable of resolving the architecture of individual lamina cribrosa beams.

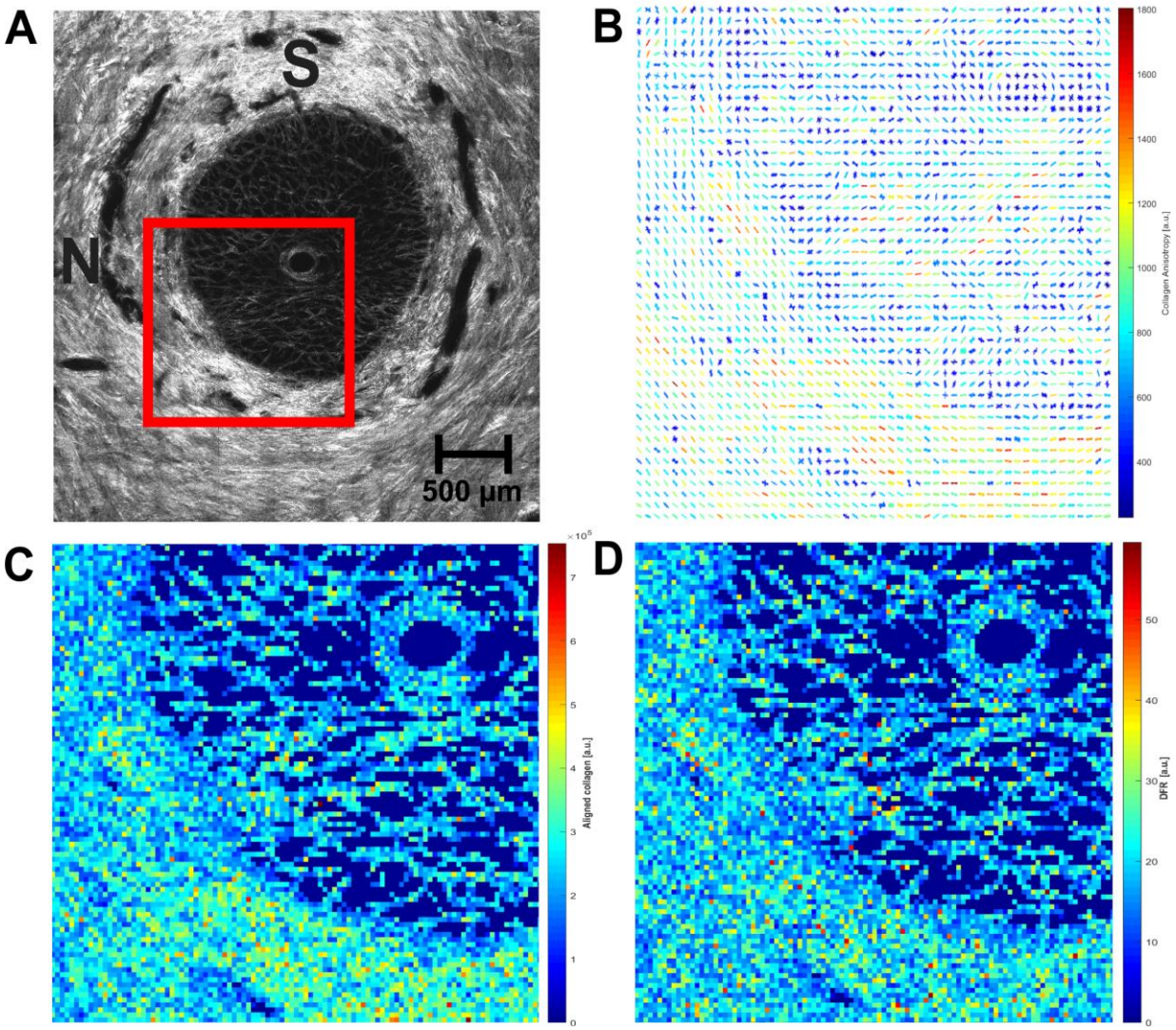

Figure 8 (A) SHG image of the adjacent optical section of the mid-stromal tissue section presented in Figure 7. (B) Polar vector map of preferential collagen fiber orientation, sampled from tiles of 32 x 32 pixels. (C) Aligned collagen map, sampled from tiles of 16 x 16 pixels. (D) Degree of fiber recruitment (DFR) map for the main collagen direction, sampled from tiles of 16 x 16 pixels. Location of maps in (B), (C) and (D) correspond to the red box bounded region in (A).

Spatial maps of aligned collagen signal (irrespective of orientation) were generated by integrating the angular distribution of the integrated power spectrum (Figures 6C, 7C and 8C). Innermost layers of the ONH reveal the areas of highest alignment corresponding to the patches of radially oriented fibres further from the scleral canal, especially in the inferior-nasal and temporal directions. With the collagen ring becoming larger and more pronounced in the mid-depth sections of the tissue, alignment increases all around the ONH, especially on

the superior and inferior side. This regional variation matches closely with areas of high fiber anisotropy (relative number of fibers aligned along the main direction).

The final fiber organization parameter mapped is the DFR for the main fiber direction (Figures 6D, 7D and 8D) which is defined by the ratio of the peak maximum to its FWHM for the largest peak. This value characterises the shape of the peak for the main fiber direction i.e. the tightness of the fiber distribution.

3.3 Validation of SHG method against WAXS

As a means of validation of the presented method in quantifying structural information from SHG images, the polar vector maps generated by our bespoke MATLAB code were compared with those obtained from the same tissue section using WAXS. WAXS is an already well-validated and established method to quantify collagen fiber organisation within connective tissue, including the sclera [19, 20, 60]. To obtain the most like-for-like correlation possible between the two methods, parameters from individual SHG optical sections (recorded every 25μm) through the physical tissue section were summed point-for-point to approximate the full-thickness sampling of the WAXS method.

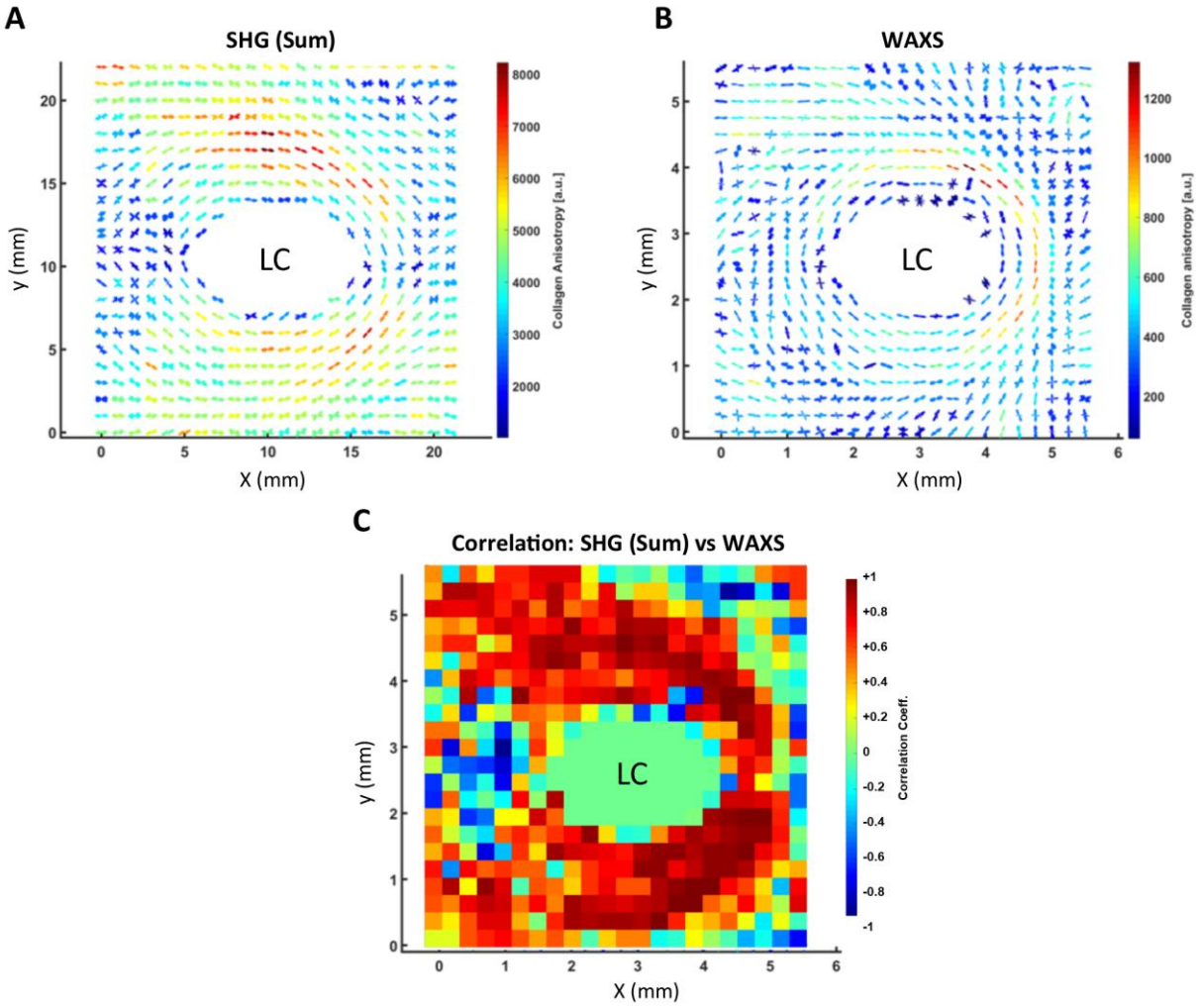

Figure 9 Comparison of PPS polar vector maps of preferential collagen fiber orientation across the same specimen using SHG and WAXS. (A) SHG data obtained by point-by-point summation of nine optical slices. (B) WAXS data obtained from single exposure that samples the full-thickness of the section. (C) Correlation map of the distribution of preferred fiber orientations in the sclera between the SHG (Sum) and WAXS data, with negative correlation coefficients (cold color shades) indicating deviation in fiber alignment between the two methods and positive correlation (warmer shades) indicating similarity (+1 indicating a perfect match and -1 indicating diametrically opposing orientations). The lamina cribrosa region (LC) is omitted from the correlation as porous tissues are difficult to assess accurately using WAXS.

Reference to Figures 9A and 9B reveals qualitatively a close overall match between the PPS polar plot maps obtained with SHG and WAXS, both methods clearly showing the presence of the collagen ring around the scleral canal, as well as the presence of an oblique fiber band emanating from the superior and inferior parts of the ring. The similarity between the structures captured with both methods was further quantified by calculating a correlation coefficient for each pair of data points that compares the full orientation distribution

(Equation 4). Large areas within the PPS exhibit strong positive correlation suggesting similar preferred directions of fibers recorded with these two methods. Weakly positive or negative correlation exist mostly in the regions where larger isotropy is observed, mainly in more peripheral regions of the specimen.

More widespread differences in the range of anisotropy (overall color-scale range of the plots) are evident between the SHG and WAXS maps (Figures 9A and B), and these are likely to have arisen from two factors. Firstly, the summed SHG signal represents only 10 – 20 μm of the total 150 μm thick section (i.e. about 10%), whereas WAXS samples every collagen fiber in the path of the X-ray beam throughout the whole tissue thickness. The variation in the individual optical slices used to obtain the integrated SHG map is shown in Fig 10, where alternative slices are presented alongside difference maps comparing the main orientation direction per polar plot in each individual slice against the corresponding values of the integrated map. Secondly, while the x-y sampling interval of 250 μm was matched for both techniques, the SHG method averaged a complete 250 x 250 μm tile, whereas the X-ray beam size sampled a smaller 150 x 80 μm area.

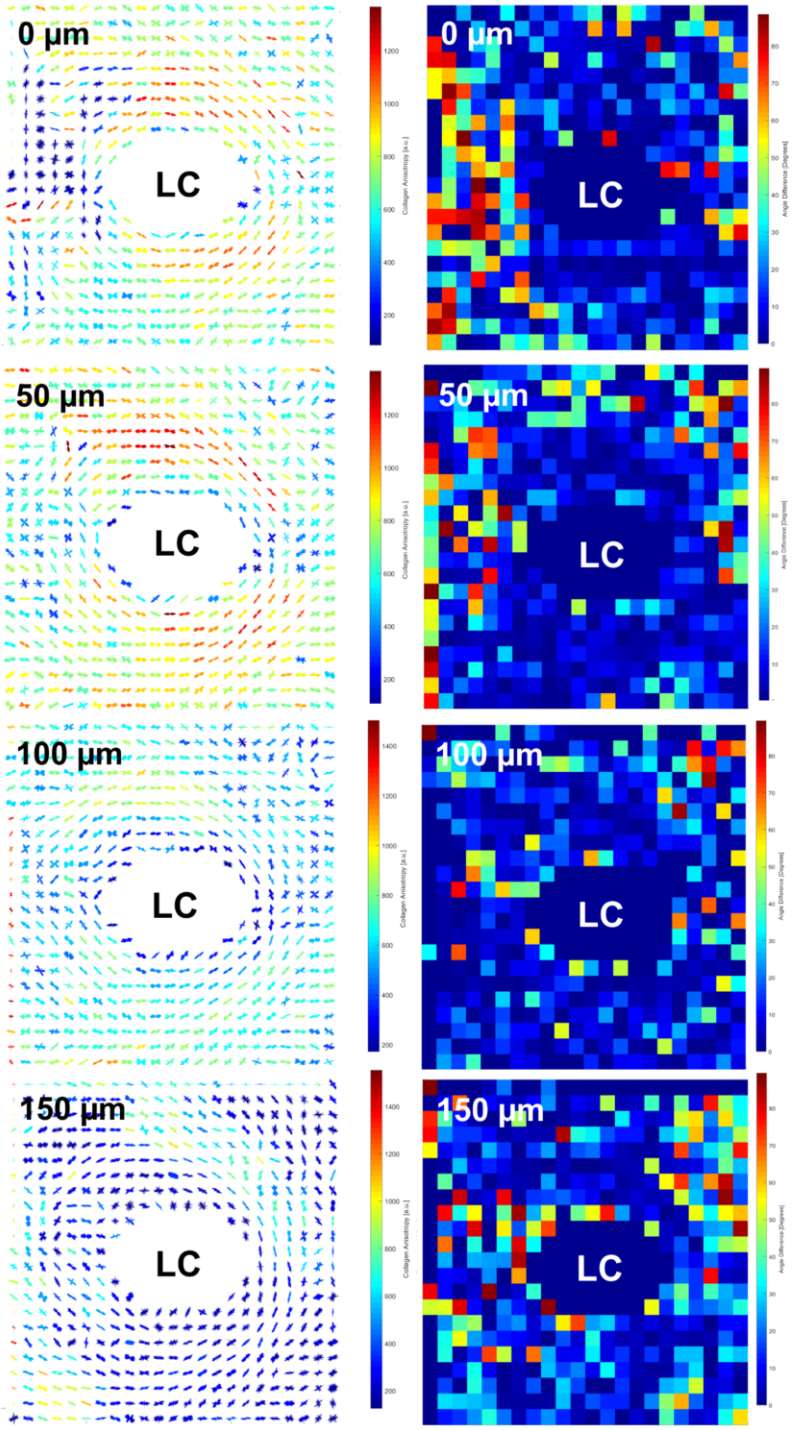

Figure 10 *Left Panel:* SHG/DFT fiber orientation data from selected optical slices through a 150µm-thick physical section of the mid-stroma of the human optic nerve head. Alternative slices of a full set of nine used to compute the summed map in Fig 9A are shown, recorded at the slice depths indicated (where 0µm indicates the top of the section and 150µm indicates the bottom). *Right Panel:* Difference in angle of the main fiber direction within each optical slice (left panel) compared to the summed map of all nine optical slices (Fig 9A).

3.4 Validation in other collagen tissues

3.4.1 Avian cornea

The avian cornea is a well-established and previously characterised model system for the study of collagen network morphogenesis [68, 69]. Studies using light/electron microscopy [70], WAXS [71] and SHG imaging [72] have shown that the mature corneal stroma in the chicken is formed from a posterior orthogonal scaffold of fibrous collagen in a fixed orientation, onto which further, successively rotated orthogonal layers (lamellae) are deposited as the tissue builds in the posterior to anterior direction during embryogenesis. As a means of further validation of the current method, we applied our quantitative SHG/DFT analysis to the mature chicken corneal stroma. Intact eye globes from adult normally sighted White Leghorn chickens, maintained at the Roslin Institute (Edinburgh, UK), were extracted immediately after sacrifice, snap frozen and stored at -80^{o}C. The corneas were dissected from the eyes immediately upon thawing and prepared for SHG imaging using identical protocols to those used for the human ONH sections (see s2.2). Details of husbandry, maintenance and ophthalmic examination of the birds may be found in a previous publication [73]. The posterior 150μm thick section (approximately two-thirds of the total ~250μm stromal thickness) was then imaged with SHG to verify the characteristic, fixed/rotated orthogonal collagen lamellar structure. 425μm × 425μm (512 ×512 pixels) FOV image z-stacks (depth interval per optical slice: 1μm) were recorded from the central corneal region of the sections, as described in s2.3. DFT analysis, following the methods presented in s2.4, was carried out using a FT image tile dimension of 64 × 64 pixels. Figure 11 shows a representative sample of the results from selected optical slices. We also computed the average polar vector plot of each optical slice (Figure 11) and used it to track the rotation of the orthogonal lamellae through the tissue depth (Figure 12). The results demonstrate that the presented method was able to detect and quantify the lamellar structure of the posterior avian cornea. Consistent with previous studies of late stage embryonic chick cornea [68, 70, 72], when traversing the stroma in a posterior to anterior direction, the deepest one-fifth (~50μm) of the adult tissue was characterised by an orthogonal collagen structure of fixed rotation, which then was observed to smoothly rotate in a counter-clockwise direction thereafter (Figures 11 and 12). Moreover, averaged polar plots of the collagen structure within each 425μm × 425μm FOV indicated that the average rotation angle for micron of stroma traversed was 1.8^{o} (Figure 12),

which is close to the values of 1.5^{o} [70] and 1.4^{o} [72] previously reported for E14 and E19 developing chick.

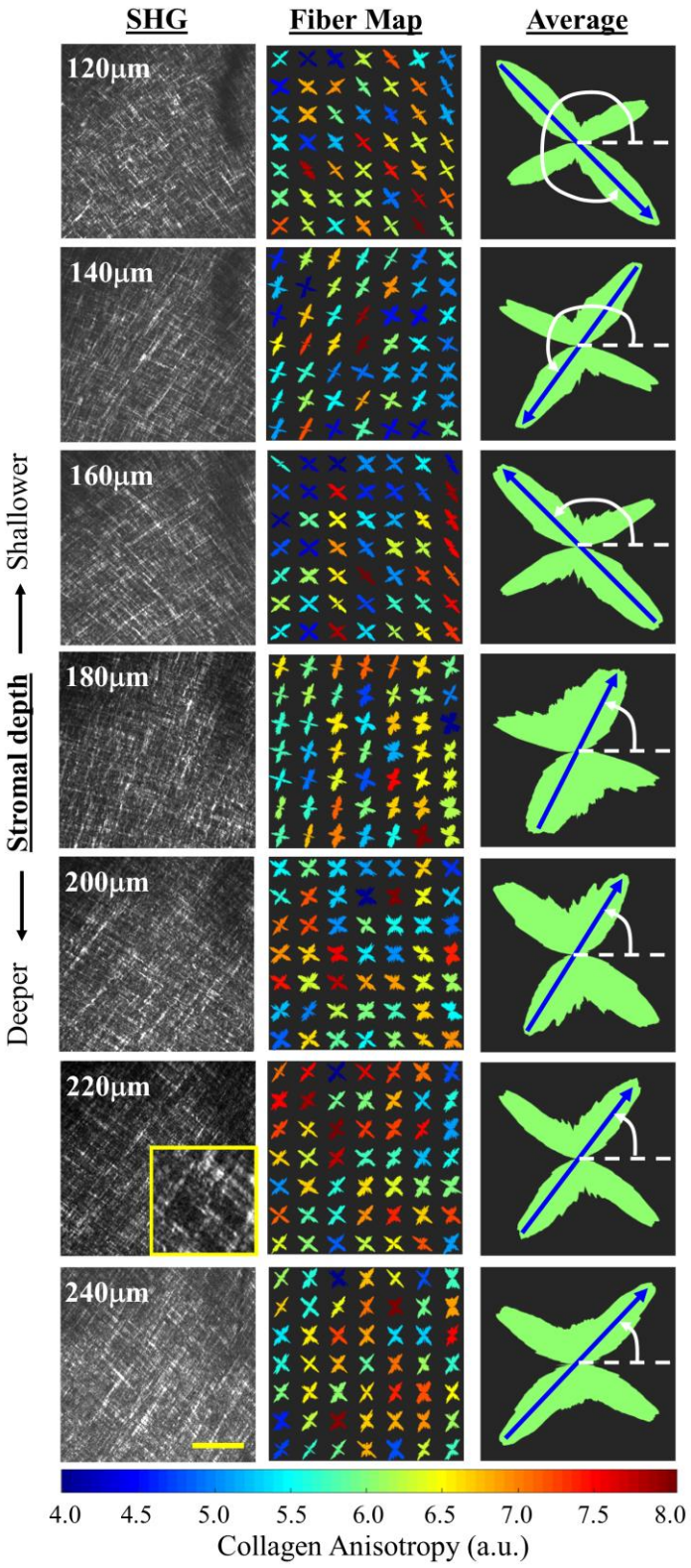

Figure 11 Depth-resolved SHG/DFT analysis of the posterior half of the corneal stroma from the adult chicken. *Left column:* SHG images reveal orthogonal collagen fiber networks (bar = 100µm). Yellow box at 220µm depth shows stroma at 3× magnification of standard images. *Centre column:* polar vector plots of collagen fiber orientation from DFT analysis (sampled every 64pix/50µm), confirming and quantifying the orthogonal lamellar structure. *Right column:* averaged polar vector plot at each

stromal depth. The fixed orientation of the deepest layers (240μm to 200μm) can be observed, followed by a counter-clockwise rotation when traversing the stroma in a posterior to anterior direction (180μm to 120 μm). The blue arrow is used to visually track the rotation angle of one of the two principal fiber populations.

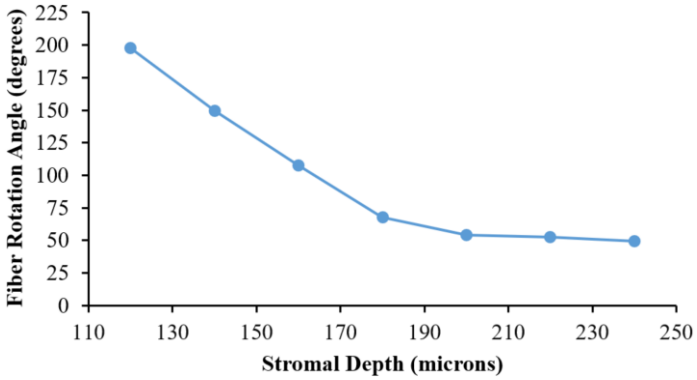

Figure 12 Measured rotation of the orthogonal collagen lamellar structure in the adult chicken corneal stroma. Fiber angle is fixed in the deepest ~50μm of the tissue, and thereafter begins to smoothly rotate in a counter-clockwise direction by an average of 1.8° for every micron of stroma traversed in the posterior to anterior direction.

3.4.2 Rat tail tendon

Rat tail tendon is a highly organised, multi-composite collagen tissue, in which collagen fibrils are assembled into fibril bundles and then into fascicles, which ultimately make up an individual tendon. The hierarchical structure of the rat tail tendon has been extensively studied by methods including electron microscopy [74, 75], X-ray scattering [74, 76] and second harmonic imaging [77, 78], revealing a highly uni-axially aligned collagen organisation in which the fibers demonstrate significant crimp in register with each other but have their long axes tightly aligned along the fascicular/tendon direction. Tails of adult Wistar rats were harvested within 1 hr of sacrifice, snap-frozen and stored at -80°C. Individual intact tendons were removed immediately upon thawing using a scalpel incision along the tail direction and extraction with fine tweezers. Short sections of tendon (~5mm long) were dissected using a scalpel and slide-mounted intact in 1:1 PBS/glycerol for SHG imaging. 425μm × 425μm (512 ×512 pixels) FOV image z-stacks (depth interval per optical slice: 1μm) were recorded from the central region of each tendon sample, as described in s2.3, and analysed using an FT tile

dimension of 16 ×16 pixel as detailed in s2.4. An example of the results is presented in Figure 13.

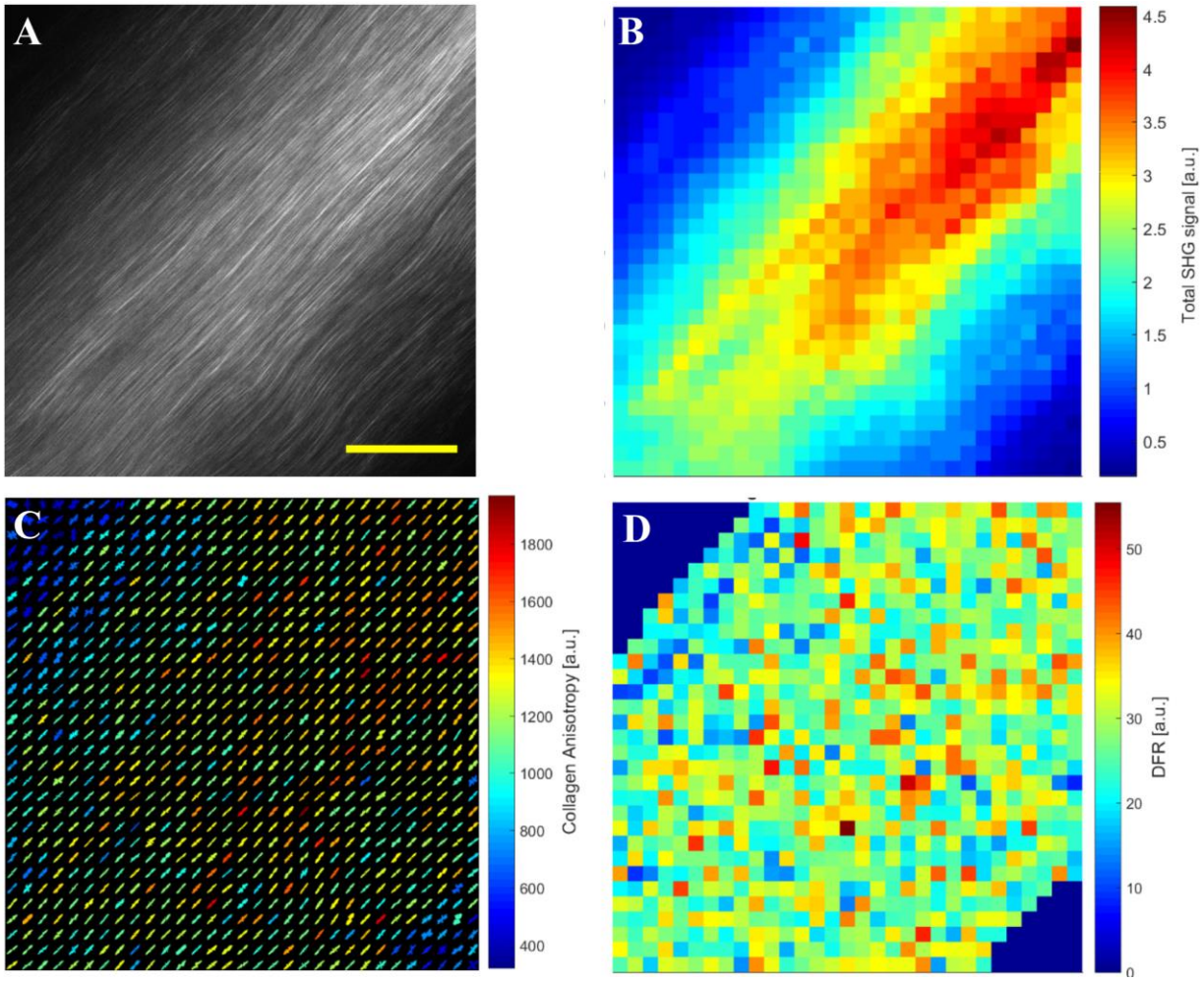

Figure 13 SHG/DFT analysis of collagen in intact rat tail tendon. (A) SHG image of single optical section through the middle of a single, intact tendon from rat tail oriented obliquely in the FOV (bar = 100μm). (B) Map of integrated SHG signal, sampled every 16pix (20μm). (C) Polar vector map of collagen fiber orientation from DFT analysis, confirming and quantifying the high uniaxial alignment of collagen along the tendon direction (D) Map of degree of fiber recruitment (DFR) around the principle fiber direction.

3.5 Application to non-collagen fiber structures: Actin cytoskeleton

In order to test the applicability of the presented DFT method to quantify non-collagenous fibrous tissues, we carried out studies of actin stress fibers induced in mechanically loaded

fibroblasts cultured from bovine sclera. Enucleated young adult bovine eyes (mean age at slaughter: 23.4 ±4.4 months) were obtained from Maddock Kembrey Meats Ltd abattoir (Maesteg, UK) immediately after slaughter. Fibroblasts were extracted and cultured from explants removed from the sclera tissue within 6 hours of animal slaughter, following protocols described elsewhere [79]. Primary cultured fibroblasts were seeded onto wells of BioFlex™ culture plates coated with type I collagen (Dunn Labortechnik, Asbach, Germany) ($0.4x10^6$ cells per well). An equibiaxial cyclic load (0.26-1.8%, 1Hz) was applied to the cells using an FX 3000 tensile system (Flexcell International, Burlington USA). Cells were fixed 6h after cessation of mechanical load and fluorescently labelled for F-actin stress fibers with Alexa-488® phalloidin (Invitrogen, Paisley, UK). Imaging was performed using a confocal laser scanning microscope (Zeiss LSM 880 with Airyscan, Carl Zeiss Ltd, Welwyn Garden City, UK) in Fast mode with a 63× oil immersion objective lens, at an image resolution of 1912x1912 pixels. DFT analysis of the F-actin stress fiber networks was performed as described in s2.4, using a 64 × 64 pixel FT tile dimension. A sample of the results is presented in Figure 14.

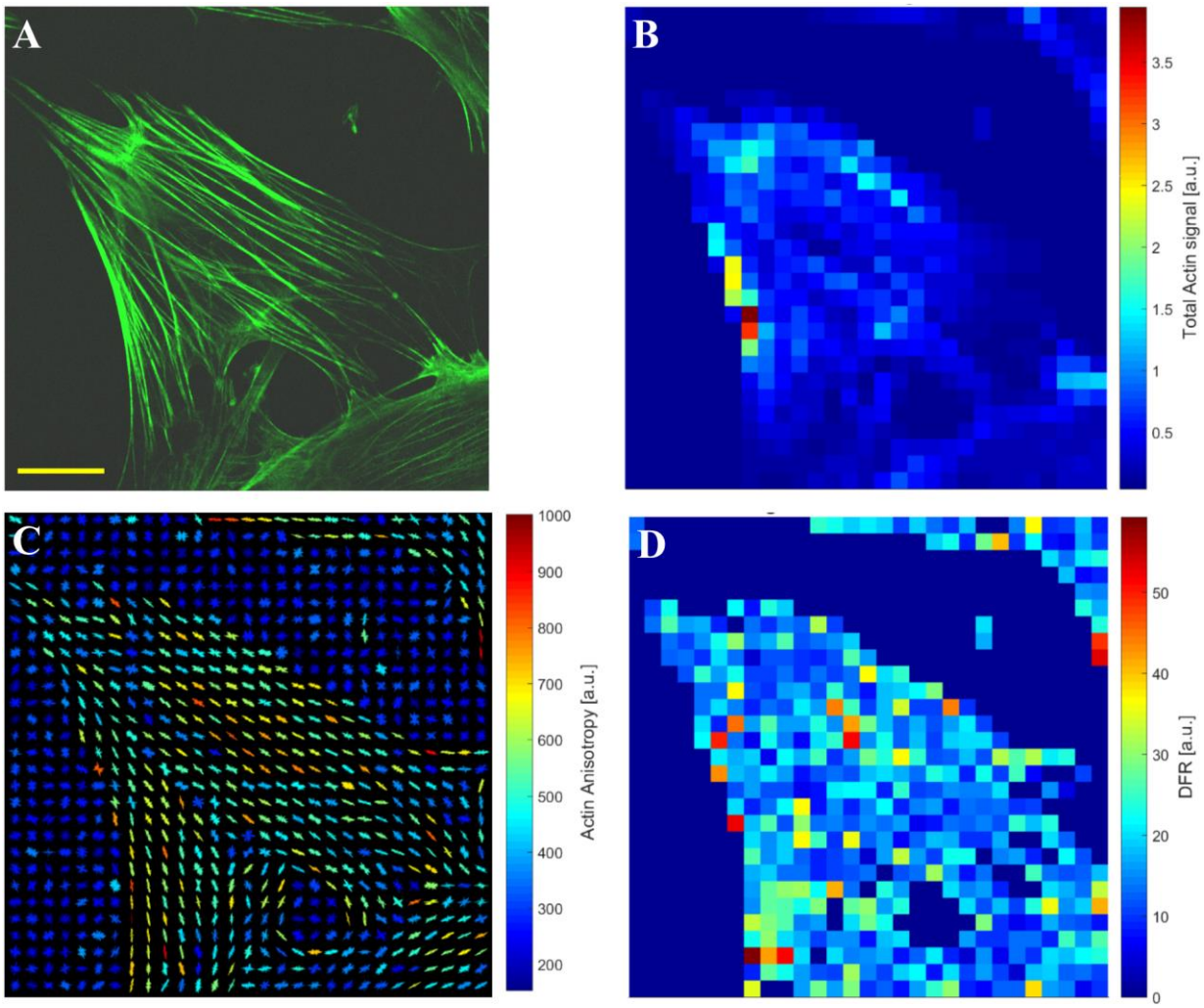

Figure 14: DFT analysis of mechanical load-induced F-actin stress fiber network in cultured bovine scleral fibroblasts imaged with fluorescence confocal microscopy. (A) Confocal image showing green cytoskeletal stress fibers of F-actin, stained with Alexa-488® phalloidin (bar = 25μm). (B) Map of integrated actin signal, sampled every 64pix (5μm). (C) Polar vector map of collagen fiber orientation from DFT analysis. (D) Map of degree of fiber recruitment (DFR) around the principle fiber direction.

4 Discussion

In this paper we describe an automated image analysis method based on tile partitioning of an SHG image and calculation the fiber structure within each tile using 2D DFT. The angular distribution of the integrated DFT power spectrum is then extracted and used to calculate and map the preferred orientation of the collagen fibers, the aligned fiber content and the degree of fiber recruitment around the main direction. The method also features an in-built correction for tile edge artefact that adopts the PPSID algorithm, avoiding the significant loss of peripheral image information encountered with commonly used alternative windowing correction methods [39], and resulting in comparatively minimal distortion of the resulting calculated fiber distribution. The latter issue has surprisingly been largely overlooked in previous studies that utilize DFT to quantify fiber organization from SHG images.

The analysis of SHG images recorded from the human ONH using our algorithm was able to quantify main collagen fiber structural features that corresponded well to previously published literature employing alternative scattering [20, 65] and imaging [64] methods. Specifically, innermost layers of the peripapillary sclera presented strong radial alignment, whereas the mid-sclera exhibited strong circumferential orientation of collagen fibers around the scleral canal. We were also able to demonstrate the applicability of the technique to image other collagen tissues by characterising the highly organised uniaxial alignment of rat tail tendon collagen and the fixed/rotated orthogonal lamellar structure of the avian cornea. Moreover, the potential for Fourier quantification of other fiber networks imaged through different imaging modalities was demonstrated by applying the presented method to fluorescence confocal images of cytoskeletal actin fiber networks in cultured fibroblasts.

As the orientation analysis approach we employed herein shows commonality with that of the WAXS analysis previously developed by our group [19, 20], we were able to carry out correlative studies to validate the former method, obtaining general agreement in the main collagen directions between the two methods when applied to the same specimens. In comparing the results of the two methods it is important to reiterate that, although the sampling intervals of the two methods used were identical (0.25mm), the actual sampled areas per data point were different (0.0625mm^2 for SHG compared to 0.012mm^2 for WAXS). Furthermore, the WAXS signal is of molecular origin and will be subject to a minor angular broadening of the orientation peak due to the ~5^o inclination of the microfibril axis with respect to the fibril direction [80]. As a further caveat, the difference in age of the two human sclera specimens studied (69 and 86) was 17 years. Based on the results of previous WAXS and finite element modelling studies [13, 20], this would not have likely resulted in any marked differences in the gross collagen fiber arrangement between the two specimens, but still could have manifested in more subtle variations in collagen anisotropy.

The option within the current method to change sampling interval (i.e. size of the image area that the DFT power spectrum is calculated, and collagen orientation is determined from) enables analysis of diverse tissue types. For example, processing SHG images with finer sampling intervals facilitates analysis of porous or fenestrated tissues such as the individual lamina cribrosa beams of the ONH, as demonstrated herein. On the other hand, mapping a continuous tissue such as the sclera with larger tile dimensions is often preferable when more regional averaging is desirable – for example to obtain representative regional parameters for biomechanical modelling. Indeed, the ability of the current method to obtain region-averaged fiber distributions with, importantly, sub-degree angular resolution, renders the data amenable to inclusion in inverse finite element simulation – as demonstrated previously with similar datasets obtained from ocular tissues using WAXS [13, 81-84]. Providing sufficient initial image resolution and effective noise filtering is obtained (in our method the latter is achieved using the MATLAB *peakprominence* function), it is feasible to analyse not only the principal fiber orientation but also additional sub-populations – for example in tissue regions where multiple fibers are crossing at different angles. This contrasts with a number of previous studies employing DFT in which only the main fiber direction is detected and the overall distribution quantified, for example by using an aspect ratio approach [31, 50, 51].

Extracting frequency component amplitudes directly from the FT power spectrum (rather than the original image) enables ready control of the frequency range (and hence corresponding length scale in the spatial domain) for analysis. This facilitates improvements in accuracy by allowing the targeting of fibers, while excluding frequencies from other structures, in order to reduce noise [49] . This could be exploited, for example, to characterize collagen fiber crimp [53]. A possible future enhancement of the current method could involve the addition of semi-automated frequency filtering to attenuate undesired radial frequencies. Marquez studied the effects of a band-pass filter and concluded that an optimal filter in concentrating DFT power on the fiber orientation is centred on frequency corresponding to a wavelength of twice the fiber width and a bandwidth of ±10% [85].

The presented work is subject to a number of limiting factors. Firstly, there are limitations inherent in the SHG tissue preparation and data collection itself. Microtome sectioning of the tissue results in mechanical disruption at the surfaces of the sections. Owing to the optical sectioning capabilities of SHG microscopy, surface data can be readily isolated and discarded, albeit at a cost of information. Further, as an imaging method, quantification of SHG can only be done from the information visible in the image section, fibers passing out of plane are not counted in the analysis, which can lead to an underestimation of signal in interwoven tissues, or where significant out-of-plane inclination of fibers is present. This is a disadvantage compared to scattering methods such as WAXS or SALS, where virtually all fibers in the plane of beam are detected. However, fine optical sections of 1 – 1.5 µm are possible with most multiphoton instruments, making tracking of inclined fibers through a section feasible if required. Also, while we used laser power ramping to effectively normalize against depth-related signal attenuation, this does rely on the assumption of isotropy in real tissue signal through a section. Any variation in the latter may manifest in some minor residual depth attenuation or over-correction throughout a section, which would impact the total SHG signal measurement in direct proportion to the attenuation factor, and (to a smaller degree) the absolute anisotropy measurement (polar plot colour scaling). However, this would not have affected the relative amount of aligned collagen, the relative number of fibres at each angle or the DFR values measured by our technique, nor would it have any effect on the spatial distribution of any measured parameter at a given section depth. Furthermore, while our SHG microscope optics achieve near-circular polarization of the beam as it exits the objective, tests

carried out on our system using an appropriate linear test sample (rat tail tendon) indicated that the polarization is marginally elliptical, resulting in a maximum bias of approximately 13% in the signal intensity in the horizontal over the vertical direction (data not shown). Secondly, there are limitations connected with our DFT analysis method. Depending on the original resolution of the SHG images collected, there is a limitation on the smallest tile that can yield a useable DFT capable of detecting fiber orientations. In the current study we obtained accurate fiber data from 16 x 16 pixel tiles with an original 512 x 512 pixel resolution image. Unlike some other methods, it is not possible to analyse signal on the single pixel level or to easily track individual collagen fibers. In this aspect, fiber tracking methods that analyse images in the spatial domain are more effective. For example, CT-FIRE and F-Segment can track fiber dimension, number and volume [45, 46], and polarization light microscopy can more effectively follow orientation [16].

In summary, this paper presents a variation on quantitative multiphoton imaging of connective tissue structure using DFT, which has two novel aspects. Firstly, it harnesses a novel PPSID algorithm to virtually eliminate peripheral data loss from image tiles during DFT analysis. Secondly, by mimicking the superior quantitative capabilities of scattering methods and combining them with the fine optical sectioning capacity of non-linear microscopy, rapid and accurate fiber quantification can be achieved, yielding data suitable for input in biomechanical modelling. In future, with the collection of optical slices at sufficiently fine resolution, and with careful and precise registration of the images, the presented method could be extended to carry out full quantitative determination of tissue organisation in three dimensions.

Acknowledgements

The authors thank Dr James Bell, Dr Lee McIlreavy and Dr Carlo Knupp (Cardiff University) for technical contributions and useful discussions, and Dr Paul Hocking (Roslin Institute) for provision of avian eye globes. This work was supported by National Institutes of Health grant R01EY021500 (subaward 2003284605). The authors also thank the Diamond Light Source for beamtime under proposal mx14757, and Diamond staff for assistance with experimental setup and data collection. Vivat Scientia Bioimaging Labs gratefully acknowledges funding

from the School of Optometry and Vision Sciences, College of Biomedical and Life Sciences and cost recovery from researchers across Cardiff University and elsewhere.

References

[1] P. G. Watson, R. D. Young *Experimental Eye Research*. **2004**, *78*, 609-623.
[2] Y. Komai, T. Ushiki *Invest Ophthalmol Vis Sci*. **1991**, *32*, 2244-2258.
[3] J. C. Downs, M. D. Roberts, C. F. Burgoyne *Optom Vis Sci*. **2008**, *85*, 425-435.
[4] H. A. Quigley, E. M. Addicks, W. R. Green, A. E. Maumenee *Arch Ophthalmol*. **1981**, *99*, 635-649.
[5] C. F. Burgoyne, J. C. Downs *J Glaucoma*. **2008**, *17*, 318-328.
[6] M. J. A. Girard, J. K. F. Suh, M. Bottlang, C. F. Burgoyne, J. C. Downs *Invest Ophthalmol Vis Sci*. **2011**, *52*, 5656-5669.
[7] I. A. Sigal, H. Yang, M. D. Roberts, C. F. Burgoyne, J. C. Downs *Invest. Ophthalmol. Vis. Sci.* **2011**, *52*, 1896-1907.
[8] R. E. Norman, J. G. Flanagan, I. A. Sigal, S. M. Rausch, I. Tertinegg, C. R. Ethier *Exp Eye Res*. **2011**, *93*, 4-12.
[9] B. Fortune, J. Reynaud, C. Hardin, L. Wang, I. A. Sigal, C. F. Burgoyne *Invest. Ophthalmol. Vis. Sci.* **2016**, *57*, 4403-4411.
[10] M. D. Roberts, Y. Liang, I. A. Sigal, J. Grimm, J. Reynaud, A. Bellezza, C. F. Burgoyne, J. C. Downs *Invest Ophthalmol Vis Sci*. **2010**, *51*, 295-307.
[11] C. Nguyen, F. E. Cone, T. D. Nguyen, B. Coudrillier, M. E. Pease, M. R. Steinhart, E. N. Oglesby, J. L. Jefferys, H. A. Quigley *Invest Ophthalmol Vis Sci*. **2013**, *54*, 1767-1780.
[12] R. Grytz, G. Meschke, J. B. Jonas *Biomech Model Mechanobiol*. **2011**, *10*, 371-382.
[13] B. Coudrillier, C. Boote, H. A. Quigley, T. D. Nguyen *Biomech Model Mechanobiol*. **2013**, *12*, 941-963.
[14] R. D. Young *Journal of Cell Science*. **1985**, *74*, 95-104.
[15] B. Yang, N. J. Jan, B. Brazile, A. Voorhees, K. L. Lathrop, I. A. Sigal *Journal of biophotonics*. **2018**, e201700356.
[16] N. J. Jan, J. L. Grimm, H. Tran, K. L. Lathrop, G. Wollstein, R. A. Bilonick, H. Ishikawa, L. Kagemann, J. S. Schuman, I. A. Sigal *Biomed Opt Express*. **2015**, *6*, 4705-4718.
[17] M. J. Girard, A. Dahlmann-Noor, S. Rayapureddi, J. A. Bechara, B. M. Bertin, H. Jones, J. Albon, P. T. Khaw, C. R. Ethier *Invest Ophthalmol Vis Sci*. **2011**, *52*, 9684-9693.
[18] H. J. Jones, M. J. Girard, N. White, M. P. Fautsch, J. E. Morgan, C. R. Ethier, J. Albon *J R Soc Interface*. **2015**, *12*.
[19] K. Meek, C. Boote *Progress in Retinal and Eye Research*. **2009**, *28*, 369-392.
[20] J. K. Pijanka, B. Coudrillier, K. Ziegler, T. Sorensen, K. M. Meek, T. D. Nguyen, H. A. Quigley, C. Boote *Invest Ophthalmol Vis Sci*. **2012**, *53*, 5258-5270.
[21] R. Cicchi, D. Kapsokalyvas, V. De Giorgi, V. Maio, A. Van Wiechen, D. Massi, T. Lotti, F. S. Pavone *Journal of biophotonics*. **2010**, *3*, 34-43.
[22] Y. Ogura, Y. Tanaka, E. Hase, T. Yamashita, T. Yasui *Experimental dermatology*. **2018**.
[23] R. M. Williams, W. R. Zipfel, W. W. Webb *Biophys J*. **2005**, *88*, 1377-1386.
[24] J. P. Wu, B. J. Swift, T. Becker, A. Squelch, A. Wang, Y. C. Zheng, X. Zhao, J. Xu, W. Xue, M. Zheng, D. Lloyd, T. B. Kirk *Journal of microscopy*. **2017**, *266*, 273-287.
[25] S. V. Plotnikov, A. C. Millard, P. J. Campagnola, W. A. Mohler *Biophysical Journal*. **2006**, *90*, 693-703.
[26] M. Winkler, D. Chai, S. Kriling, C. J. Nien, D. J. Brown, B. Jester, T. Juhasz, J. V. Jester *Invest Ophthalmol Vis Sci*. **2011**, *52*, 8818-8827.
[27] M. Han, G. Giese, J. Bille *Opt Express*. **2005**, *13*, 5791-5797.

[28] C. Y. Park, C. M. Marando, J. A. Liao, J. K. Lee, J. Kwon, R. S. Chuck *Invest Ophthalmol Vis Sci*. **2016**, *57*, 5602-5610.
[29] M. P. Rubbens, A. Driessen-Mol, R. A. Boerboom, M. M. Koppert, H. C. van Assen, B. M. TerHaar Romeny, F. P. Baaijens, C. V. Bouten *Ann Biomed Eng*. **2009**, *37*, 1263-1272.
[30] J. S. Bell, A. O. Adio, A. Pitt, L. Hayman, C. E. Thorn, A. C. Shore, J. L. Whatmore, C. P. Winlove *Am J Physiol Heart Circ Physiol*. **2016**, *311*, H1560-H1568.
[31] P. Matteini, F. Ratto, F. Rossi, R. Cicchi, C. Stringari, D. Kapsokalyvas, F. S. Pavone, R. Pini *Optics Express*. **2009**, *17*, 4868-4878.
[32] N. Morishige, R. Shin-Gyou-Uchi, H. Azumi, H. Ohta, Y. Morita, N. Yamada, K. Kimura, A. Takahara, K. H. Sonoda *Invest Ophthalmol Vis Sci*. **2014**, *55*, 8377-8385.
[33] S. J. Lin, W. Lo, H. Y. Tan, J. Y. Chan, W. L. Chen, S. H. Wang, Y. Sun, W. C. Lin, J. S. Chen, C. J. Hsu, J. W. Tjiu, H. S. Yu, S. H. Jee, C. Y. Dong *J Biomed Opt*. **2006**, *11*, 34020.
[34] R. Tanaka, S. Fukushima, K. Sasaki, Y. Tanaka, H. Murota, T. Matsumoto, T. Araki, T. Yasui *J Biomed Opt*. **2013**, *18*, 61231.
[35] O. Nadiarnykh, R. B. LaComb, M. A. Brewer, P. J. Campagnola *BMC Cancer*. **2010**, *10*, 94-94.
[36] B. Wen, K. R. Campbell, K. Tilbury, O. Nadiarnykh, M. A. Brewer, M. Patankar, V. Singh, K. W. Eliceiri, P. J. Campagnola *Scientific Reports*. **2016**, *6*, 35734.
[37] K. R. Campbell, P. J. Campagnola in Assessing local stromal alterations in human ovarian cancer subtypes via second harmonic generation microscopy and analysis, Vol. 22 (Ed.^Eds.: Editor), SPIE, City, **2017**, pp.7.
[38] A.-M. Pena, A. Fabre, D. Débarre, J. Marchal-Somme, B. Crestani, J.-L. Martin, E. Beaurepaire, M.-C. Schanne-Klein *Microscopy Research and Technique*. **2007**, *70*, 162-170.
[39] M. Yildirim, K. P. Quinn, J. B. Kobler, S. M. Zeitels, I. Georgakoudi, A. Ben-Yakar *Scanning*. **2016**, *38*, 684-693.
[40] P. J. Campagnola, L. M. Loew *Nat Biotechnol*. **2003**, *21*, 1356-1360.
[41] W. R. Zipfel, R. M. Williams, W. W. Webb *Nat Biotechnol*. **2003**, *21*, 1369-1377.
[42] F. J. Avila, J. M. Bueno *Applied optics*. **2015**, *54*, 9848-9854.
[43] R. Rezakhaniha, A. Agianniotis, J. T. Schrauwen, A. Griffa, D. Sage, C. V. Bouten, F. N. van de Vosse, M. Unser, N. Stergiopulos *Biomech Model Mechanobiol*. **2012**, *11*, 461-473.
[44] A. Boudaoud, A. Burian, D. Borowska-Wykręt, M. Uyttewaal, R. Wrzalik, D. Kwiatkowska, O. Hamant *Nature protocols*. **2014**, *9*, 457.
[45] J. Wu, B. Rajwa, D. L. Filmer, C. M. Hoffmann, B. Yuan, C. Chiang, J. Sturgis, J. P. Robinson *Journal of microscopy*. **2003**, *210*, 158-165.
[46] A. M. Stein, D. A. Vader, L. M. Jawerth, D. A. Weitz, L. M. Sander *Journal of microscopy*. **2008**, *232*, 463-475.
[47] K. P. Quinn, I. Georgakoudi *J Biomed Opt*. **2013**, *18*, 046003.
[48] J. S. Bredfeldt, Y. Liu, C. A. Pehlke, M. W. Conklin, J. M. Szulczewski, D. R. Inman, P. J. Keely, R. D. Nowak, T. R. Mackie, K. W. Eliceiri *J Biomed Opt*. **2014**, *19*, 16007.
[49] E. A. Sander, V. H. Barocas *Journal of biomedical materials research. Part A*. **2009**, *88*, 322-331.
[50] W. Lo, W.-L. Chen, C.-M. Hsueh, A. A. Ghazaryan, S.-J. Chen, D. H.-K. Ma, C.-Y. Dong, H.-Y. Tan *Invest. Ophthalmol. Vis. Sci.* **2012**, *53*, 3501-3507.
[51] A. Ghazaryan, H. F. Tsai, G. Hayrapetyan, W. L. Chen, Y. F. Chen, M. Y. Jeong, C. S. Kim, S. J. Chen, C. Y. Dong *J Biomed Opt*. **2013**, *18*, 31105.
[52] C. Bayan, J. M. Levitt, E. Miller, D. Kaplan, I. Georgakoudi *Journal of applied physics*. **2009**, *105*, 102042.
[53] W. Lee, H. Rahman, M. E. Kersh, K. C. Toussaint, Jr. *Journal of biomedical optics*. **2017**, *22*, 46009.
[54] O. Marques in *Frequency-Domain Filtering, Vol.* (Ed. O. Marques), **2011**.
[55] R. C. Gonzalez, R. E. Woods, S. L. Eddins in *Filtering in the Frequency Domain, Vol.*, McGraw Hill Education (India), **2011**.
[56] R. Hovden, Y. Jiang, H. L. Xin, L. F. Kourkoutis *Microscopy and Microanalysis*. **2015**, *21*, 436-441.
[57] A. Kim, N. Lakshman, W. M. Petroll *Experimental Cell Research*. **2006**, *312*, 3683-3692.

[58] W. Burger, M. J. Burge in *The Discrete Fourier Transform in 2D, Vol.*, Springer-Verlag London, **2008**, pp.352-358.
[59] L. Moisan *Journal of Mathematical Imaging and Vision*. **2011**, *39*, 161-179.
[60] C. Boote, J. R. Palko, T. Sorensen, A. Mohammadvali, A. Elsheikh, A. M. Komaromy, X. Pan, J. Liu *Molecular vision*. **2016**, *22*, 503-517.
[61] J. K. Pijanka, A. Abass, T. Sorensen, A. Elsheikh, C. Boote *Journal of Applied Crystallography*. **2013**, *46*, 1481-1489.
[62] J. K. Pijanka, E. C. Kimball, M. E. Pease, A. Abass, T. Sorensen, T. D. Nguyen, H. A. Quigley, C. Boote *Invest. Ophthalmol. Vis. Sci.* **2014**, *55*, 6554-6564.
[63] J. S. Bell, S. Hayes, C. Whitford, J. Sanchez-Weatherby, O. Shebanova, C. Vergari, C. P. Winlove, N. Terrill, T. Sorensen, A. Elsheikh, K. M. Meek *Acta Biomaterialia*. **2018**, *65*, 216-225.
[64] N.-J. Jan, K. Lathrop, I. A. Sigal *Invest. Ophthalmol. Vis. Sci.* **2017**, *58*, 735-744.
[65] J. K. Pijanka, M. T. Spang, T. Sorensen, J. Liu, T. D. Nguyen, H. A. Quigley, C. Boote *PLoS ONE*. **2015**, *10*, e0118648.
[66] I. A. Sigal, J. G. Flanagan, K. L. Lathrop, I. Tertinegg, R. Bilonick *Invest Ophthalmol Vis Sci*. **2012**, *53*, 6870-6879.
[67] R. Ren, N. Wang, B. Li, L. Li, F. Gao, X. Xu, J. B. Jonas *Invest Ophthalmol Vis Sci*. **2009**, *50*, 2175-2184.
[68] E. Koudouna, M. Winkler, E. Mikula, T. Juhasz, D. J. Brown, J. V. Jester *Prog Retin Eye Res*. **2018**, *64*, 65-76.
[69] A. J. Quantock, M. Winkler, G. J. Parfitt, R. D. Young, D. J. Brown, C. Boote, J. V. Jester *Exp Eye Res*. **2015**, *133*, 81-99.
[70] R. L. Trelstad, A. J. Coulombre *The Journal of cell biology*. **1971**, *50*, 840-858.
[71] A. J. Quantock, C. Boote, V. Siegler, K. M. Meek *Investigative Ophthalmology & Visual Science*. **2003**, *44*, 130-136.
[72] E. Koudouna, E. Mikula, D. J. Brown, R. D. Young, A. J. Quantock, J. V. Jester *Acta biomaterialia*. **2018**, *79*, 96-112.
[73] C. Boote, S. Hayes, S. Jones, A. J. Quantock, P. M. Hocking, C. F. Inglehearn, M. Ali, K. M. Meek *J Struct Biol*. **2008**, *161*, 1-8.
[74] J. Kastelic, A. Galeski, E. Baer *Connect Tissue Res*. **1978**, *6*, 11-23.
[75] R. W. Rowe *Connect Tissue Res*. **1985**, *14*, 9-20.
[76] F. Bianchi, F. Hofmann, A. J. Smith, M. S. Thompson *Acta biomaterialia*. **2016**, *45*, 321-327.
[77] C. H. Lien, K. Tilbury, S. J. Chen, P. J. Campagnola *Biomedical optics express*. **2013**, *4*, 1991-2002.
[78] K. Reiser, P. Stoller, A. Knoesen *Scientific reports*. **2017**, *7*, 2642.
[79] B. Molik, PhD Thesis, Cardiff University, **2016**.
[80] S. Yamamoto, H. Hashizume, J. Hitomi, M. Shigeno, S. Sawaguchi, H. Abe, T. Ushiki *Archives of Histology and Cytology*. **2000**, *63*, 127-135.
[81] B. Coudrillier, J. Pijanka, J. Jefferys, T. Sorensen, H. A. Quigley, C. Boote, T. D. Nguyen *J Biomech Eng*. **2015**, *137*.
[82] B. Coudrillier, J. Pijanka, J. Jefferys, T. Sorensen, H. A. Quigley, C. Boote, T. D. Nguyen *J Biomech Eng*. **2015**, *137*, 041006.
[83] B. Coudrillier, J. K. Pijanka, J. L. Jefferys, A. Goel, H. A. Quigley, C. Boote, T. D. Nguyen *PLoS One*. **2015**, *10*, e0131396.
[84] C. Whitford, H. Studer, C. Boote, K. M. Meek, A. Elsheikh *J Mech Behav Biomed Mater*. **2015**, *42*, 76-87.
[85] J. P. Marquez *International Journal of Solids and Structures*. **2006**, *43*, 6413-6423.